Article

Magnetic Carbon Foam Adorned with Co/Fe Nanoneedles as an Efficient Activator of Oxone for Oxidative Environmental Remediation: Roles of Surficial and Chemical Enhancement

Yi-Chun Chen [1,2,†], Xin-Yu Jiang [3,†], Bui Xuan Thanh [4,5], Jia-Yin Lin [6], Haitao Wang [7], Chao-Wei Huang [8], Hongta Yang [9,*], Afshin Ebrahimi [10,11], Sanya Sirivithayapakorn [12] and Kun-Yi (Andrew) Lin [3,13,*]

1   Department of Civil Engineering, National Taipei University of Technology, Taipei City 10608, Taiwan
2   Department of Biotechnology, National Formosa University, Yunlin 63208, Taiwan
3   Department of Environmental Engineering, Innovation Increasepment Center of Sustainable Agriculture, National Chung Hsing University, Taichung 402, Taiwan
4   Faculty of Environment and Natural Resources, Ho Chi Minh City University of Technology (HCMUT), Ho Chi Minh City 700000, Vietnam
5   Key Laboratory of Advanced Waste Treatment Technology, Vietnam National University Ho Chi Minh (VNU-HCM), Linh Trung Ward, Ho Chi Minh City 700000, Vietnam
6   Semiconductor and Green Technology Program, National Chung Hsing University, 250 Kuo-Kuang Road, Taichung 402, Taiwan
7   Key Laboratory of Pollution Processes and Environmental Criteria, College of Environmental Science and Engineering, Nankai University, Tianjin 300071, China
8   Department of Engineering Science, National Cheng Kung University, Tainan 70101, Taiwan
9   Department of Chemical Engineering, National Chung Hsing University, Taichung 402, Taiwan
10 Department of Environmental Health Engineering, School of Health, Isfahan University of Medical Sciences, Isfahan 81676-36954, Iran; a_ebrahimi@hlth.mui.ac.ir
11 Environment Research Center, Research Institute for Primordial Prevention of Non-Communicable Disease, Isfahan University of Medical Sciences, Isfahan 81746-73461, Iran
12 Environmental Engineering Department, Faculty of Engineering, Kasetsart University, Bangkok 10900, Thailand; fengsys@ku.ac.th
13 Institute of Analytical and Environmental Sciences, National Tsing Hua University, Hsinchu 40227, Taiwan
*   Correspondence: hyang@nchu.edu.tw (H.Y.); linky@nchu.edu.tw (K.-Y.L.)
†   These authors contributed equally to this work.

Abstract: As heterogeneous catalysis is a practical method for activating Oxone, the immobilization of transition metals (e.g., Co, Fe) on carbonaceous supports is a promising platform. Thus, this study attempts to develop a carbon-supported metallic catalyst by growing Co/Fe on carbon foam (CF) via adopting melamine foam as a readily available template which could be transferred to nitrogen-doped CF with marcoporous structures. Specifically, a unique adornment of Co/Fe species on this CF is facilely fabricated through a complexation of Co/Fe with a plant extract, tannic acid, on melamine foam, followed by carbonization to produce nano-needle-like Co/Fe on N-doped CF, forming a magnetic CF (MCF). This resultant MCF exhibits a much higher surface area of 54.6 m^2/g than CF (9.5 m^2/g), and possesses a much larger specific capacitance of 9.7 F/g, than that of CF as 4.0 F/g. These superior features of MCF enable it to accelerate Oxone activation in order to degrade an emerging contaminant, bis(4-hydroxyphenyl)methanone (BHPM). Furthermore, MCF + Oxone exhibits a lower activation energy as 18.6 kJ/mol for BHPM elimination and retains its effectiveness in eliminating BHPM over multiple rounds. More importantly, the CF is also prepared and directly compared with the MCF to study the composition-structure-property relationship to provide valuable insights for further understanding of catalytic behaviors, surficial characteristics, and application of such a functional carbon material.

Keywords: carbon; foam; magnetic; $CoFe_2O_4$; Oxone

1. Introduction

Chemical oxidation techniques are versatile processes not only for decontaminating polluted water by degrading pollutants [1–4] but also for various oxidative chemical syntheses [1,2]. Typically, chemical oxidation techniques involve strong oxidation-power species, such as reactive oxygen species (ROS), to oxidize organic pollutants or molecules. Today, hydroxyl radical ($^{\bullet}$OH) is one of the most common ROS and has been extensively employed for the degradation of contaminants via the so-called Fenton's reaction [3,4] and oxidative synthesis of target compounds [1,2]. Nevertheless, sulfate radicals (e.g., $SO_4^{\bullet-}$) are also being increasingly developed for the aforementioned applications owing to several benefits of $SO_4^{\bullet-}$, such as a comparable or even greater oxidation power, greater selectivity, wider operational pH ranges, longer half-lives, etc. [5].

For generating $SO_4^{\bullet-}$, two types of commercial reagents are usually used, namely, persulfate (PS) ($S_2O_8^{2-}$) and Oxone (SO_5^{2-}). Nevertheless, both PS and Oxone require proper "activation" to release "$SO_4^{\bullet-}$" from these reagents [6]. Because Oxone can be activated by many methods and exhibits a superior capacity for degrading organic pollutants [7], it has been favorably adopted recently specifically for decontamination of toxic pollutants as well as oxidative organic synthesis [2].

While many approaches can activate Oxone [8–11], catalytic activation is considered the most useful and efficient technique [12]. Specifically, using transition metals (e.g., Co, Fe, Mn, etc.) for Oxone activation is even more promising [1]. Nevertheless, direct use of these metal species may encounter several problems, including different recovery of metals, secondary contamination by these metals, and poor reusability, etc. [13,14]. Thus, heterogeneous catalysts are increasingly proposed for activating Oxone, and immobilizing metal species on substrates appears as a viable platform to afford a useful "activator" for Oxone in order to degrade pollutants efficiently [12].

To this end, carbonaceous materials have been proven as ideal substrates because carbon is the most earth-abundant element and offers easy accessibility, high conductivity, and durable stability [15,16]. For instance, Xu et al. developed a graphene-based $CoFe_2O_4$ for activating Oxone and found a superior synergy between graphene and $CoFe_2O_4$ [17]. Some other studies have also reported the usage of activated carbon for supporting Co/Fe nanoparticles, affording composite catalysts for enhancing Oxone activation [18].

Therefore, it would be promising to establish carbon-supported heterogeneous catalysts. In particular, since Oxone activation for the degradation of pollutants is a catalytic reaction in aqueous media, optimal heterogeneous catalysts are anticipated to offer high accessibility by exhibiting porous structures. Therefore, foamy materials should be attractive supports, and carbon foam (CF) would be an excellent candidate.

Fabrication of CF actually can be achieved by using 3-dimensional (3D) organic templates, followed by carbonization, to retain the 3D porous foam, affording a carbonaceous substrate [19]. Moreover, such a CF can even be functionalized to exhibit magnetism, converting CF to magnetic CF (MCF), which can be easily manipulated by external magnetic forces for facilitating recovery and increasing recyclability [19]. More importantly, by endowing magnetism onto the CF to become MCF, metal species (i.e., the source of magnetism) can also be adorned onto the CF, and these metal species (e.g., Co and Fe) would be active sites for activating Oxone. Therefore, the present study proposes the usage of melamine foam as a precursor to generate CF as melamine foam that actually is made up of nitrogen groups, and this melamine foam-derived CF would afford N-doped CF. The literature has further indicated that the hetero-atom-dopant on carbon materials would also act as additional active sites for participating in Oxone activation [20].

Furthermore, in order to immobilize metal species on melamine foam, a unique method is proposed here through the complexation of metals with tannic acid (TA), an extract from natural plants, onto surfaces of melamine foam. In particular, because Co and Fe are recognized as the most efficient transition metals for activating Oxone [1,15], the complexation of Co/Fe by TA would enhance the immobilization of Co/Fe on the melamine foam.

Specifically, an emerging contaminant, bis(4-hydroxyphenyl)methanone (BHPM), is chosen as a model pollutant and organic compound here because BHPM is a popular ultra-violet light stabilizer, which has been widely added to various products to prevent the harmful effects of sunlight. However, BHPM is validated as an endocrine disruptor, which would threaten the aquatic ecology once released into the water environment. Thus, the degradation of BHPM by the proposed MCF-activated Oxone would be employed to investigate properties of the MCF, and detailed studies of BHPM degradation via experimental and theoretical investigations would also be provided.

More importantly, the CF (without metal complexations) would also be prepared and directly compared with this MCF to study the composition-structure-property relationship and provide valuable insights into further understanding of catalytic behaviors, surficial characteristics, and application of such a functional carbon material. More interestingly, the complexation of Co/Fe with TA would lead to the growth of specially shaped Co/Fe materials (i.e., thorns and needles) on the CF to increase the accessibility of Oxone to these active sites by increasing the surface area/porosity. Therefore, through this study, a MCF with useful Co/Fe active species and superior structural, textural, and magnetic properties can be established.

2. Experimental

The procedure of fabricating MCF is outlined and displayed in Figure 1. The preparation process of MCF is illustrated as displayed in Figure 1. Typically, cobalt chloride (0.1 mmol), iron chloride (0.1 mmol), and 0.2 mmol of tannic acid (TA) were added to the 100 mL of DI water [21], into which a piece of melamine foam (1 cm × 1 cm × 1 cm) was placed. Subsequently, the mixture was adjusted to achieve pH = 8 and then aged for 15 min to allow the complexation of Co/Fe with TA on the pristine foam. The Co/Fe-TA-modified foam was rinsed using water and ethanol, and then carbonized at 600 °C in the N_2 atmosphere to afford Co/Fe-deposited carbon foam.
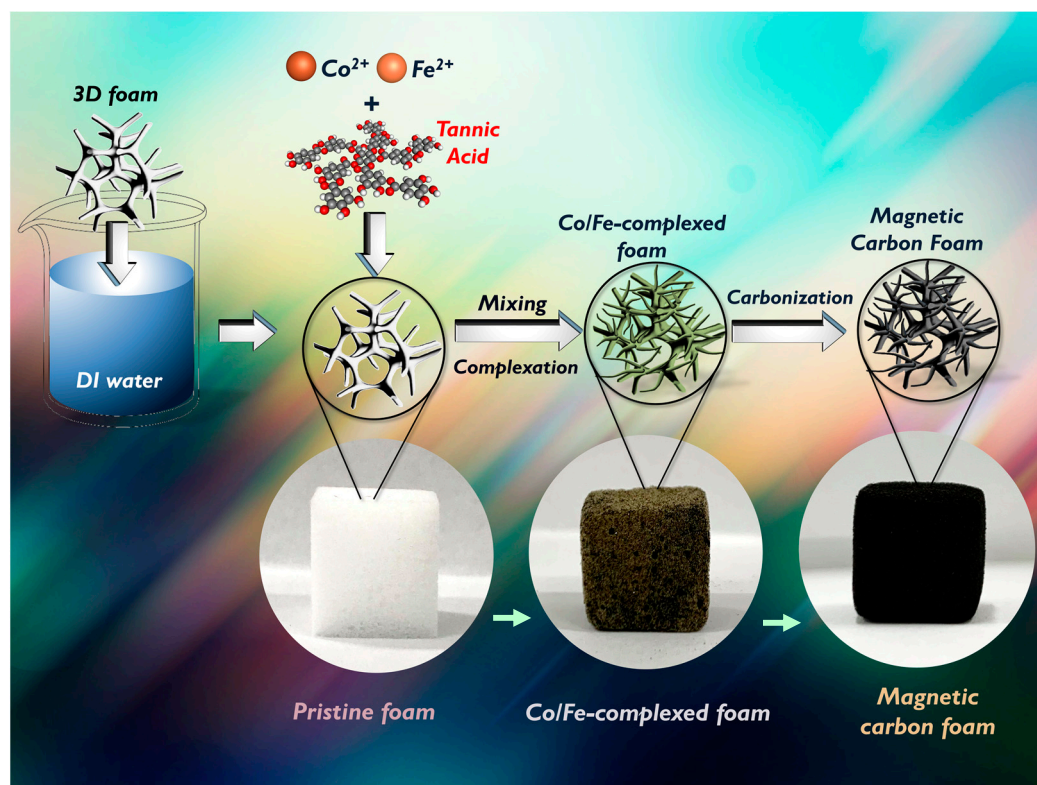
Figure 1. Preparation scheme for MCF via the complexation of Co^{2+}, Fe^{2+}, and TA.

For characterizations, the appearance of the as-prepared materials was firstly visualized by SEM (JEOL JSM-7800 F, Tokyo, Japan). The crystalline structures of materials were also verified by an X-ray diffractometer (Bruker, Billerica, MA, USA). Furthermore, the chemical states of elements in the as-prepared materials were also characterized by X-ray photoelectron spectroscopy (XPS) (PHI 5000, ULVAC-PHI, Kanagawa, Japan). Additionally, the physical properties of catalysts were analyzed by a volumetric analyzer (Anton Paar Auto IQ, Graz, Austria).

The BHPM elimination by Oxone, characterization techniques, and theoretical analysis can be found in the supporting information. To evaluate the elimination kinetics, the equation below is frequently employed and adopted here for quantification of the rate constant, *k*:

$$Ln(C_t/C_0) = -kt \tag{1}$$

where C_0 is an initial concentration of BHPM and C_t is the concentration of BHPM at a certain reaction time "*t*".

3. Results and Discussion

3.1. Properties of MCF

Morphologies and Compositional Analyses

Because MCF was derived from the melamine foam, it would be interesting to observe the variation in the bulky appearance from the pristine foam to the MCF. Figure 1 shows the preparation procedure as well as the actual picture of the pristine foam, which was cut to afford a cube with a completely white color. One can also notice that such a pristine foam had the nature of foam with noticeable pores (Figure 2a). After immersing this foam into the Co/Fe-TA mixture, the white foam had become brownish, and the foam was noticeably adorned with fine substances (the inset in Figure 1). Once this brownish foam was further carbonized, it finally became completely black as shown in Figure 2b, suggesting that the pristine foam had changed to a carbonaceous material. In addition, the microscale appearances of these materials are also visualized in Figure 2. Specifically, Figure 2c shows the typical triangular frame of the melamine foam, which exhibited a smooth and clean surface. Nevertheless, once such a pristine foam has been pyrolyzed in an air-lean atmosphere, the triangular frame can still be retained (Figure 2d); however, one can note that the surface of the frame has become coarse with wrinkles, signifying that the carbonized foam (CF) itself can remain intact. Furthermore, after the deposition of Co/Fe-TA on the foam, followed by carbonization, the entire cubic foam remained as a cubic black material as shown in Figure 2b, and microscopically, the triangular framework still remained (Figure 2d); interestingly, many thorn- or needle-like substances were adorned on the frame.

The composition of such a needle-adorned carbon foam was then measured in Figure 2f, in which strong signals of C, N, O, Fe and Co could be detected, suggesting that the resultant black foam was made up of these elements, becoming a carbon foam accompanied by Fe/Co/N/O constituents.

Moreover, the crystalline structures of these materials were also analyzed. Initially, the pristine foam exhibited a relatively amorphous pattern (Figure 3a), whereas the carbonized foam (CF) also revealed a very weak signal of carbon at 26.8°. Nevertheless, once Co/Fe-TA complexation with the foam took place, followed by carbonization, the resultant material was then also analyzed to exhibit multiple peaks.
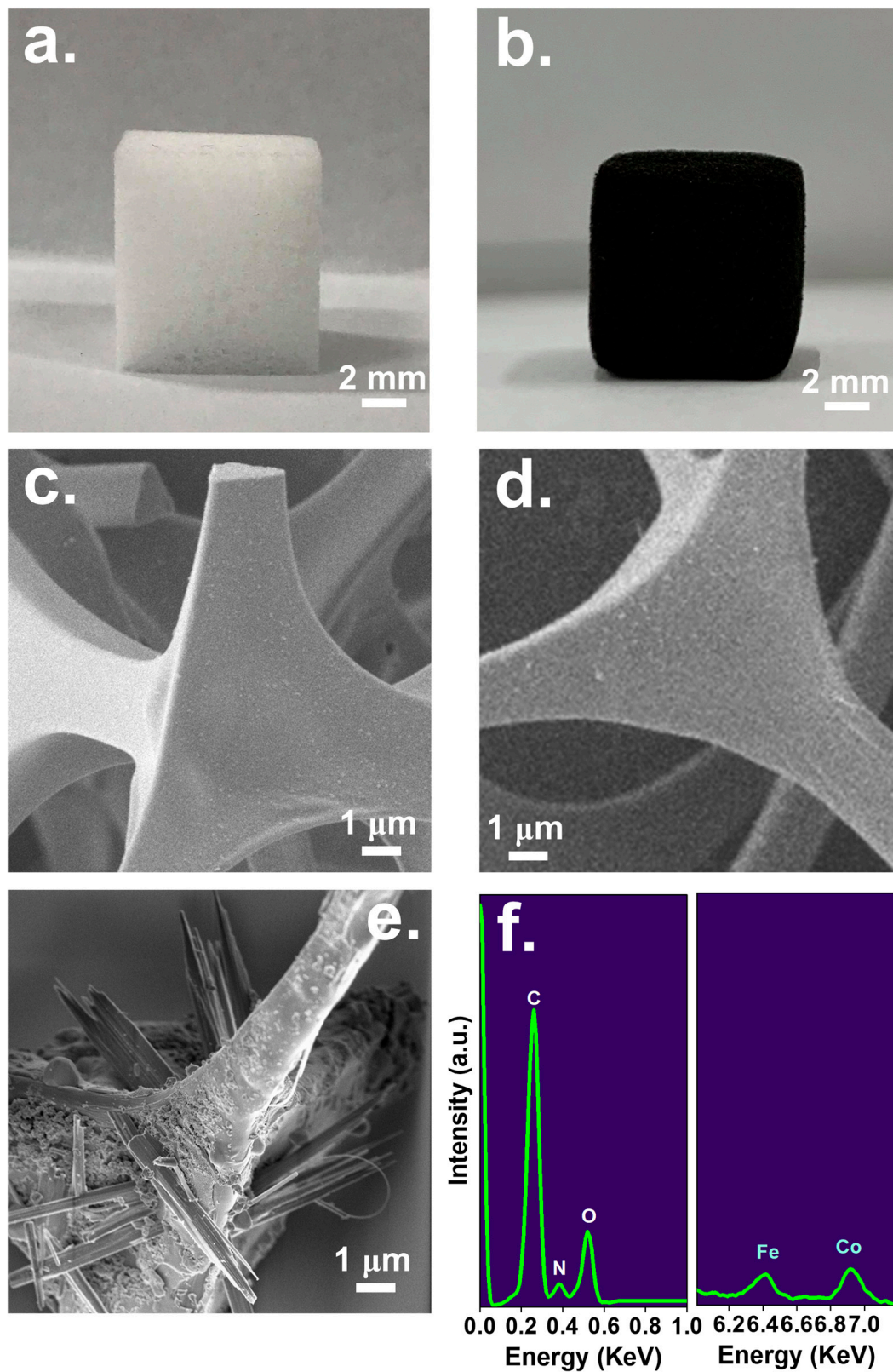
Figure 2. Pictures of (**a**) pristine foam and (**b**) the resultant MCF; electronic microscopic images of (**c**) pristine foam, (**d**) carbonized foam (CF), and (**e**) MCF and (**f**) its composition.
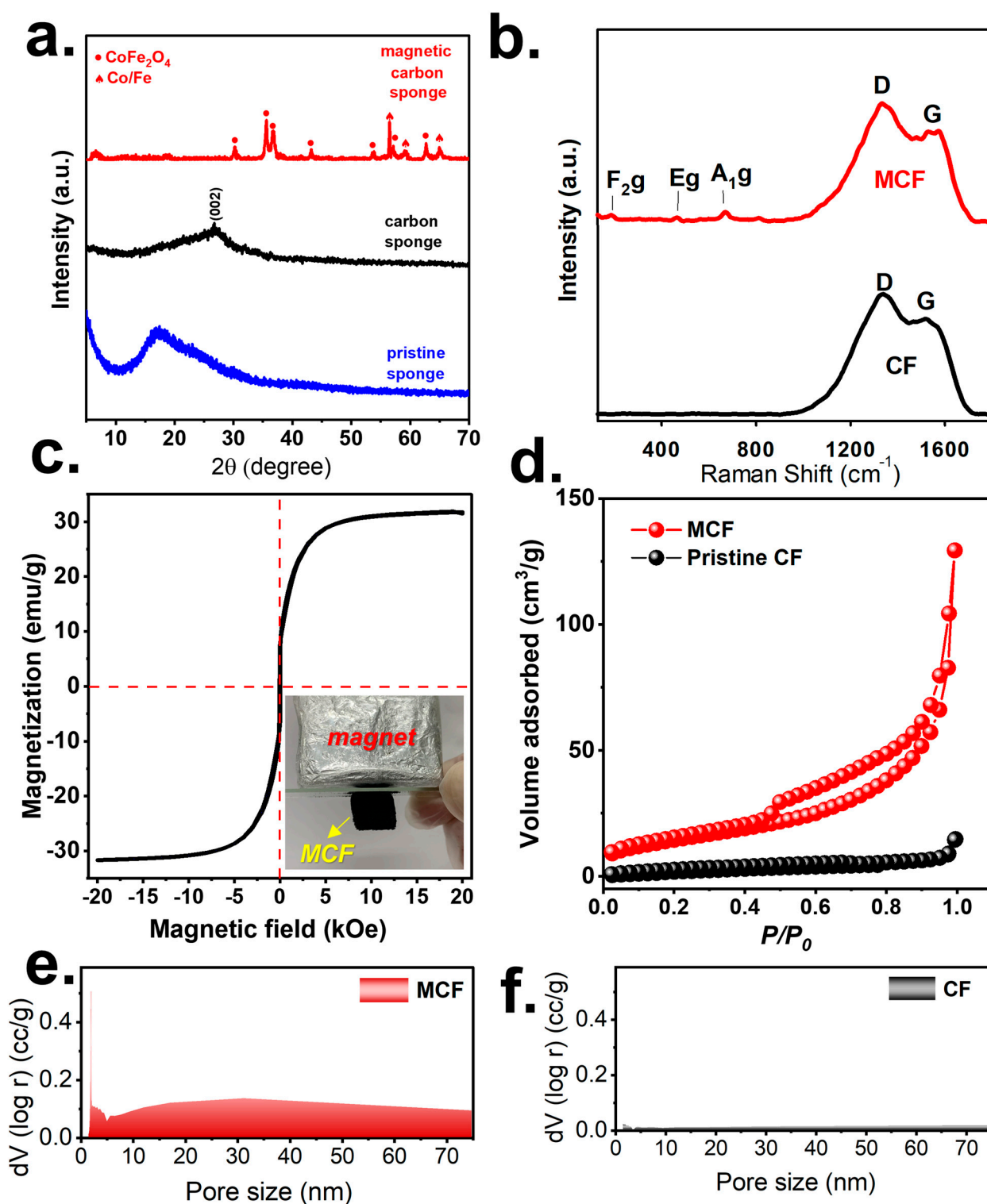
Figure 3. (**a**) XRD patterns; (**b**) Raman analyses, (**c**) saturation magnetization of MCF, (**d**) N_2 sorption isotherms, (**e**,**f**) pore size distributions of CF and MCF.

In particular, the noticeable peaks can also be found at 30.2°, 35.5°, 36.8°, 41.5°, 43.2°, 53.7°, 57.2°, and 62.7°; this could be well indexed to $CoFe_2O_4$ (JCPDS #03-0864), suggesting that Co and Fe were combined and oxidized to afford such a bimetallic oxide. Furthermore, a few peaks can also be observed at 56.5°, 59.2°, and 65.0° that could be attributed to the metallic phases of Co or Fe (JCPDS #65-9722).

Additionally, the resultant material was then further characterized using Raman spectroscopy as shown in Figure 3b. In the case of the simple CF (without the Co/Fe-TA complexation), its Raman spectrum consisted of noticeable bands at 1340 and 1520 cm^{-1}, corresponding to the D and G bands of the conjugated carbon, confirming that the pristine foam after carbonization would become CF. On the other hand, the Raman spectrum of this needle-adorned CF also contained the noticeable D and G bands, validating the existence of carbon substrate in this modified foam. Furthermore, several relatively minor bands can also be observed in the low-wavelength range at around 190, 470, and 670 cm^{-1}, that correspond to the F_2g, E_g, and A_1g of metals [22], thereby confirming the existence of the Co/Fe species in such a modified foam.

Owing to the presence of $CoFe_2O_4$ and Co/Fe, such a modified CF could exhibit magnetism; therefore, its magnetization was measured in Figure 3c, in which the saturation magnetization could approach 31 emu/g, confirming that this modified CF was a magnetic CF (MCF), and such a magnetization allowed this MCF to be manipulated by an external magnet for withdrawal and releasing as shown in Figure 3d.

Figure 3c further shows its adsorption result which could be categorized as an IUPAC IV sorption with a notable hysteresis loop, indicating that the MCF exhibited mesopores. Simultaneously, Figure 3e also reveals the N_2 sorption of the CF, which was actually similar to that of the MCF but with a much smaller N_2 sorption volume. As the surface area of the MCF was then determined as 54.6 m^2/g, the CF merely showed a surface area of 9.5 m^2/g, demonstrating that the adornment of needles on the MCF enabled it to exhibit much more surface area. On the other hand, Figure 3f also reveals the pore size distribution of the MCF, in which a large fraction of pores in the mesoscale range could be observed, and the total pore volume was 0.21 cc/g, whereas the total pore volume of the CF was merely 0.01 cc/g. This result also corroborates the much superior textural property of the MCF over the CF to provide more contact areas.

3.2. Degradation of BHPM by MCF + Oxone

Degradation of BHPM by Oxone using the MCF was then measured in Figure 4. Because the BHPM might be removed by sorption, the sorption of the BHPM on the MCF was then studied. However, the BHPM was barely removed using the MCF; thus, the BHPM was not eliminated by sorption. On the other hand, by using Oxone alone, the BHPM was only slightly degraded (~5%) in 30 min. Yet, as the MCF and Oxone would be both adopted simultaneously, the concentration of the BHPM dropped quickly in 30 min, indicating that the MCF may activate the Oxone to eliminate the BHPM. For comparison with the MCF, the industrially available Co_3O_4 powder (Figure S1) and CF were also employed to activate the Oxone and eliminate the BHPM as in Figure 4a. Nevertheless, Co_3O_4 + Oxone enabled C_t/C_0 to reach 0.39 after 30 min, while CF+Oxone led to $C_t/C_0 = 0.69$. Both Co_3O_4 and CF were capable of activating the Oxone; however, their catalytic activities were clearly much lower than the MCF.

To quantitatively measure the BHPM elimination kinetics, the rate constants (k values) for the BHPM degradation are then summarized in Figure 4b. The k for MCF + Oxone would be 0.169 min^{-1}, which was much larger than the k values of Co_3O_4+Oxone (i.e., 0.035 min^{-1}) and CF+Oxone (0.012 min^{-1}), indicating that the MCF was certainly superior to the industrial Co_3O_4 and CF. This was possibly because the industrial Co_3O_4 powder was highly aggregated and typically exhibits very low surface areas due to agglomeration as shown in Figure S1.

Because the MCF led to the much quicker degradation of the BHPM, it was also essential to probe into how the Oxone was "consumed" by the MCF. In Figure 4c, Oxone consumption during BHPM degradation was inspected. In 30 min, ~70% of Oxone was "consumed" by the MCF, while Oxone consumptions by CF and Co_3O_4 were substantially lower (33% and 20%, respectively). It was worth comparing the k values of Oxone consumption that are then summarized in Figure 4d. The k using the MCF was 0.063 min^{-1}, the k by CF was 0.009 min^{-1} and that by Co_3O_4 was 0.017 min^{-1}, corroborating that the

Oxone consumption by the MCF was considerably quicker and more effective than the CF and Co_3O_4, thereby leading to the quicker BHPM elimination.
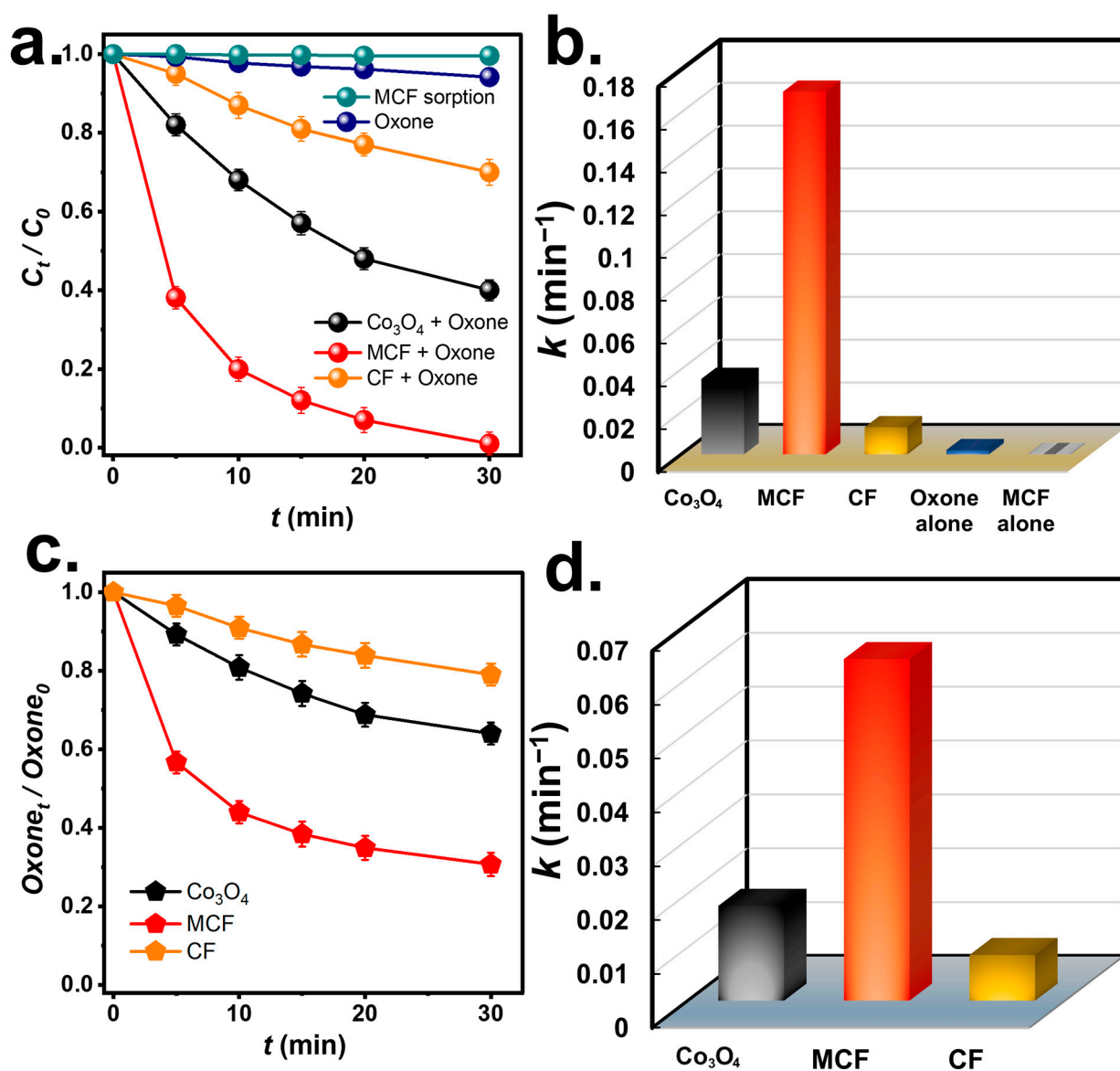
Figure 4. (**a**) Comparison of degradation of BHPM and (**b**) corresponding rate constants of BHPM degradation; (**c**) comparison of Oxone consumption and (**d**) rate constants of Oxone consumption (Catalyst = 200 mg/L, Oxone = 200 mg/L, T = 30 °C).

As Oxone activation is relevant to surficial reactions between Oxone and catalysts, it was necessary to further characterize the surficial properties of the MCF. Therefore, in Figure 5, X-ray photoelectron spectroscopy (XPS) results of MCF are measured and depicted. Specifically, the C1s result of the MCF (Figure 5a) could be resolved to multiple peaks at 284.1, 286.6, and 288.5 eV, ascribed to the C-C, C-N, and C=O moieties [23]. Moreover, the Co2p result of the MCF would be disintegrated to afford several peaks (Figure 5b). Particularly, the peak at 778.4 eV was Co^0, whereas the peaks at 780.1 and 795.3 eV were indexed to Co^{2+} and the peaks at 782.9 and 796.3 eV were attributed to Co^{3+} [24].
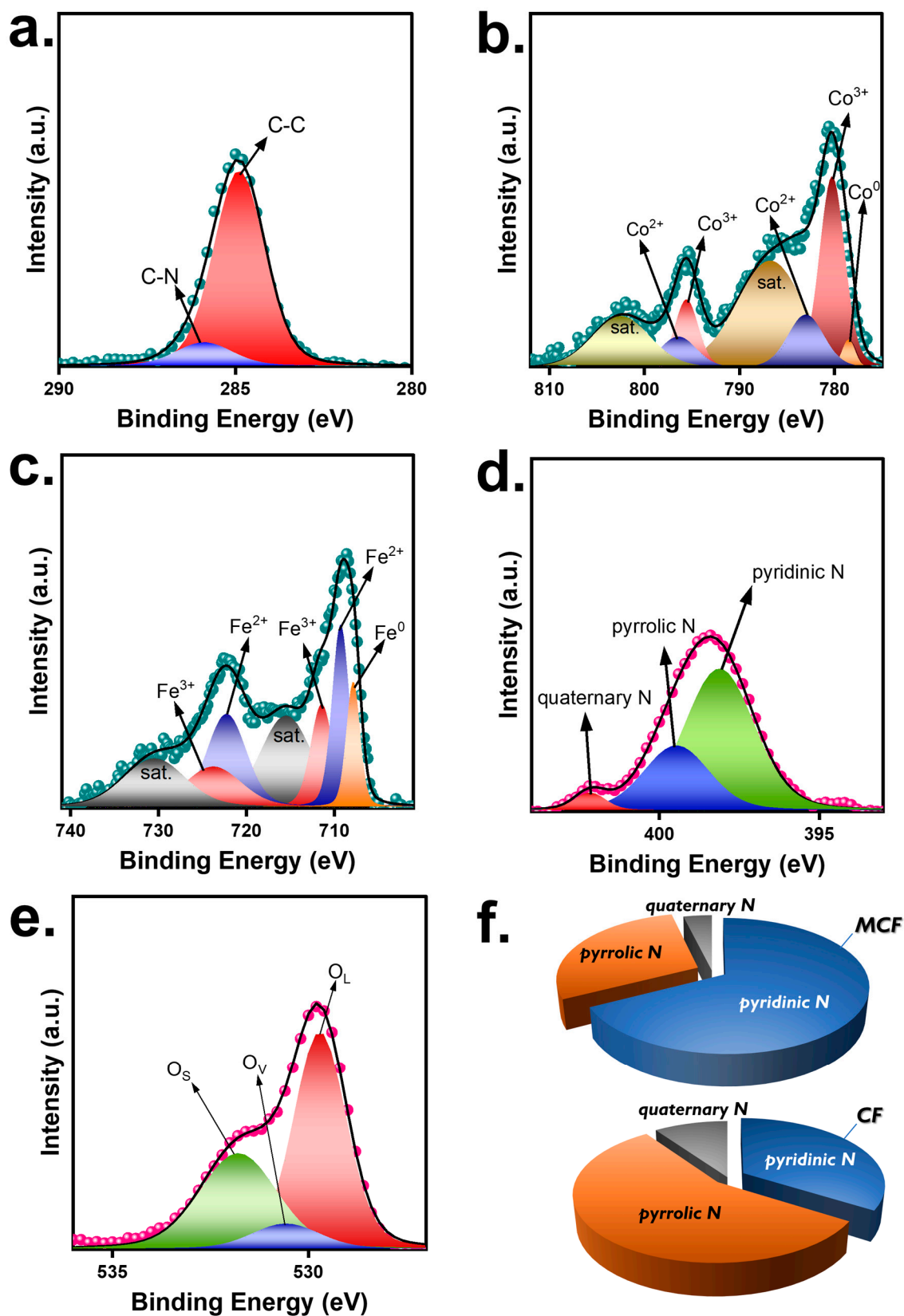
Figure 5. (**a**–**e**) XPS analyses of MCF; (**f**) fractions of N species in MCF and CF.

Furthermore, the Fe2p curve of the MCF (Figure 5c) was also deconvoluted to afford a series of peaks, and specifically, the peak at 707.6 eV corresponds to Fe^0 [25,26]. Fur-

thermore, the peaks at 709.2 and 722.1 eV would be ascribed to Fe^{2+}, while the peaks at 711.3 and 723.6 eV would be ascribed to Fe^{3+} [25,26]. On the other hand, the N1s curve of the MCF was also obtained and analyzed (Figure 5d) to reveal several peaks at 398.1, 399.4, and 402.0 eV, attributed to the pyridinic N, pyrrolic N, and quaternary N group in the MCF [27], confirming that the CF was certainly doped by N from the carbonization of melamine foam and that the fraction of N in the MCF was 3.4%. In addition, the O1s curve of the MCF was then measured to reveal the oxygenic species in the MCF and the curve can be deconvoluted to show three underlying peaks at 529.6, 530.6, and 531.8 eV, corresponding to the O_L (lattice), O_V (vacancy), and O_S (sorbed), respectively [28].

Comparatively, the XPS results of the CF were also measured and are displayed in Figure S2. In particular, the C1s curve of the CF also exhibited C-C, C-N, and C-O species, indicating the existence of an N-doped carbonaceous matrix. Moreover, Figure S2b also reveals the N1s in the CF, in which the pyridinic N, pyrrolic N, and quaternary N can be clearly observed. However, the fractions of these species seemed to differ from those seen in the MCF.

Specifically, the MCF consisted of pyridinic N, pyrrolic N, and quaternary N of 67.4%, 28.8%, and 3.8%, respectively, while the CF showed pyridinic N, pyrrolic N, quaternary N of 33.9%, 56.2%, 9.9%, respectively. As pyridinic N is confirmed as highly effective for Oxone activation [29], the much higher pyridinic N species in the MCF (i.e., 67.4%) than in the CF (33.9%) could lead to promoting catalytic activities of the MCF for activating Oxone in the BHPM decomposition.

More importantly, the MCF was constituted of various metal species of Co/Fe that would serve as much more active sites for activating Oxone, thereby accelerating Oxone decomposition and then BHPM elimination [30,31].

On the other hand, Oxone activation would also be associated with redox properties. Therefore, the electrochemical properties of MCF as well as CF were then analyzed. Figure 6a displays the cyclic voltammetry (CV) curves of the MCF and CF. The CF showed a much smaller CV loop, while the MCF revealed a larger CV loop. Therefore, the MCF possessed a much larger specific capacitance of 9.7 F/g, which was much higher than that of the CF as 4.0 F/g. This comparison confirms that MCF possessed superior redox characteristics and was expected to enhance faster interfacial processes than CF [32].
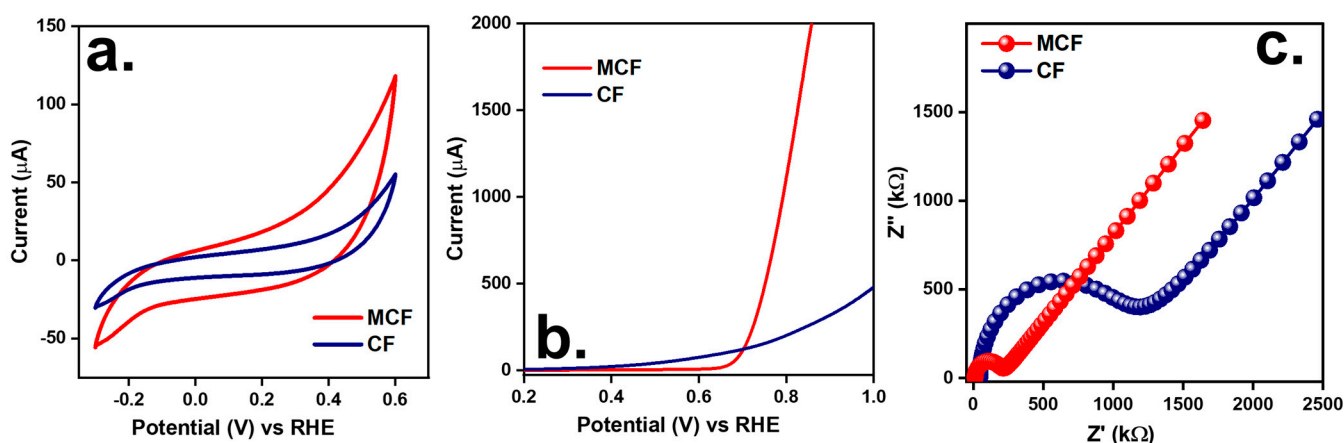
Figure 6. Electrochemical properties of MCF and CF: (**a**) CV curves, (**b**) LSV curves, (**c**) EIS Nyquist plots.

In comparison to the pristine CF, the MCF was intentionally prepared to consist of transition metals (i.e., Co and Fe) that would exhibit high theoretical specific capacitance, thereby making the MCF possess a much higher specific capacitance than the pristine CF as Co/Fe was distributed and adorned on the CF [33].

Moreover, the linear sweep voltammogram (LSV) results of the MCF and CF are shown in Figure 6b. The MCF necessitated a much smaller initial potential than the CF to reach the same current level, indicating that the MCF possessed superior electrical transport

properties than the CF. Besides, an analysis of the charge transfer in the MCF and CF was implemented by looking into their Nyquist plots (Figure 6c). When comparing MCF and CF, the MCF showed a significantly narrower semi-circle in the high-frequency area than the CF, suggesting that the MCF possessed a higher degree of charge transfer and lower resistivity [34]. This was possibly because the adornment of Co/Fe on the CF substantially increased its conductivity and supplied more active sites for an electrochemical reaction process [35].

In view of these comparisons, MCF, owing to the adornment of Co/Fe species, exhibited superior porous characteristics and more active surfaces as well as improved electrochemical features, making MCF an enhanced activator for Oxone to accelerate Oxone decomposition and then BHPM degradation.

3.3. BHPM by MCF + Oxone: Other Effects

As MCF + Oxone eliminated the BHPM effectively, the temperature and pH would also impact BHPM degradation. Figure 7a shows BHPM removal by MCF + Oxone from 30 to 50 °C. As the temperature rose from 30 to 40 °C, the k value for BHPM degradation rose from 0.170 min^{-1} to 0.215 min^{-1}. When it increased to 50 °C, the rate constant of BHPM degradation rose to 0.267 min^{-1}, indicating the enhancing effect of elevated temperatures on BHPM elimination. Furthermore, these rate constants at different temperatures were correlated using the Arrhenius equation as follows [36]:

$$\ln k = \ln A - \frac{E_a}{RT} \tag{2}$$

where E_a denotes the activation energy of BHPM degradation; it was calculated as 18.6 kJ/mol, which is significantly smaller than the E_a values of BHPM elimination in the literature (Table S1) [37]. These comparisons further demonstrate that MCF was a superior activator for Oxone to degrade BHPM.

Additionally, the effect of the initial pH on BHPM elimination is further studied in Figure 7b. At the typical pH = 7, BHPM was degraded speedily with $k = 0.170$; however, once the pH was lowered to pH = 5, the rate constant diminished to 0.080 min^{-1}. At pH = 3, BHPM degradation became even slower with $k = 0.020$ min^{-1}. This is possibly because the low-pH condition affords an H^{+-}abundant environment, where H$^+$ tends to consume potential radicals to "annihilate" them through the following reactions:

$$H^+ + SO_4^{\bullet -} + e^- \rightarrow HSO_4^- \tag{3}$$

$$H^+ + {}^{\bullet}OH + e^- \rightarrow H_2O \tag{4}$$

Moreover, Oxone may also become dull under acidic conditions [38], then leading to ineffective BHPM elimination.

On the other hand, when the solution became alkaline at pH = 9, BHPM elimination was also retarded with a smaller k of 0.047 min^{-1}. At pH = 11, BHPM degradation was almost completely inhibited to afford an extremely low k of 0.001 min^{-1}. Such a negative effect of the strongly alkaline condition may be because the *pKa* value of Oxone is 9.4, and thus the electrostatic revulsion was more intense between the Oxone and MCF, leading to the ineffective degradation [38].
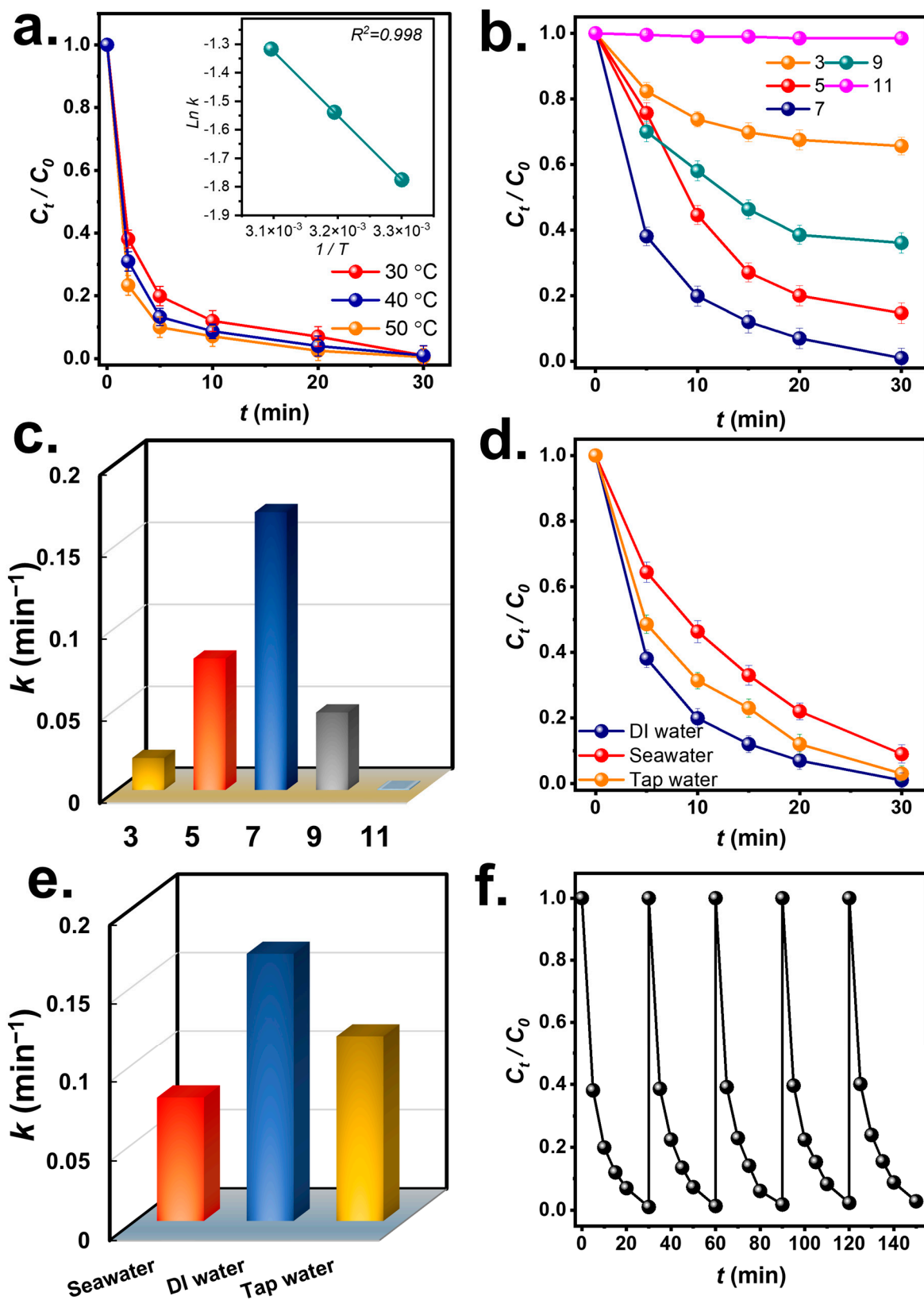
Figure 7. Effects of various factors on BHPM degradation by MCF + Oxone: (**a**) temperature, (**b**,**c**) pH and corresponding rate constants, (**d**,**e**) aquatic media and corresponding rate constants (DI water: deionized water); (**f**) recyclability.

Since BHPM may be present in different water media, it was worth investigating how water media would influence the efficacy of BHPM degradation. Therefore, in addition to DI water, tap water and seawater were then also adopted as water matrices, as in Figure 7d. With tap water, the beginning of BHPM elimination with $k = 0.116$ min^{-1} was still very efficient. Tap water may contain impurities but the efficiency of BHPM elimination was still reasonable, as BHPM could be successfully and almost completely eliminated. In the case of seawater, the slightly lower k value of 0.078 min^{-1} was obtained as seawater contains a large number of substances and impurities, such as Cl$^-$, which has been validated to interfere with Oxone by reacting with radicals to form lower-oxidation-potential ROS, leading to a less efficient BHPM degradation [39].

As MCF can competently eliminate BHPM, the reusability of MCF to eliminate BHPM over several rounds was evaluated. Figure 7f depicts that the MCF could eliminate BHPM over five consecutive rounds. This result corroborates the theory that the spent MCF can maintain its efficacy for activating Oxone to degrade BHPM. The XRD analysis of the spent MCF (Figure S3) shows that it remained almost comparable, demonstrating that the MCF would be a reusable activator.

3.4. Mechanistic Studies by MCF + Oxone

For further unraveling the degradation mechanism, a few probe agents were then employed for elucidating the ROS during the BHPM degradation. At first, *t*-butyl alcohol (BuOH) was used to be a probe agent for $^\bullet$OH, while methanol (MeOH) was used to identify the presence of both SO$_4^{\bullet-}$ and $^\bullet$OH. After TBA was added to the solution, the BHPM degradation proceeded noticeably slower (Figure 8a), and the k decreased from 0.170 to 0.040 min^{-1} (Figure 8b), signifying that $^\bullet$OH occurs during BHPM elimination. Next, as MeOH was used, the BHPM elimination was substantially inhibited with $k = 0.001$ min^{-1}, signifying that SO$_4^{\bullet-}$ and $^\bullet$OH co-exist in BHPM elimination. Furthermore, benzoquinone (BQ) was adopted to examine superoxide (O$_2^{\bullet-}$). Figure 8a reveals that BQ inhibited the BHPM elimination with $k = 0.106$ min^{-1}, demonstrating that the contribution of O$_2^{\bullet-}$ to BHPM elimination may be insignificant.

In order to examine the occurrence of O$_2^{\bullet-}$, an alternative analytic technique was then adopted here by using nitro blue tetrazolium (NBT) as an indicator of O$_2^{\bullet-}$ because NBT could be reduced selectively by O$_2^{\bullet-}$ to monoformazan, which would absorb the visible light at 530 nm. However, Figure S4 further depicts the fact that while NBT itself exhibited the peaks at 259 and 330 nm, the spectral variation did not show noticeable bands of monoformazan at 530 nm after Oxone was added, suggesting that O$_2^{\bullet-}$ was negligible and its contribution to BHPM degradation would be quite marginal. Nevertheless, the low k of BHPM seen in the case of the addition of BQ may be because BQ consumed a part of the Oxone without generating ROS, thereby leading to the slightly retarded BHPM degradation. Moreover, NaN$_3$ was used to study singlet oxygen (^{1}O$_2$), and NaN$_3$ also inhibited BHPM elimination with $k = 0.036$ min^{-1}, revealing that ^{1}O$_2$ is also present from MCF + Oxone.

The occurrence of these radicals at different reaction times was then determined. Specifically, Figure 8c shows the variations in SO$_4^{\bullet-}$ and $^\bullet$OH as a function of the reaction time. Nevertheless, the concentration of SO$_4^{\bullet-}$ seemed much higher than that of $^\bullet$OH, which agrees with the above-mentioned discussions.

Furthermore, the occurrence of ^{1}O$_2$ was associated with furfuryl alcohol (FFA) consumption [40]. Figure 8c reveals the FFA oxidation by using Oxone alone and MCF + Oxone. Oxone alone seemed to barely lead to FFA consumption, whereas MCF + Oxone led to significant oxidation of the FFA, suggesting that MCF would cause the consumption of Oxone and promote the production of ^{1}O$_2$.
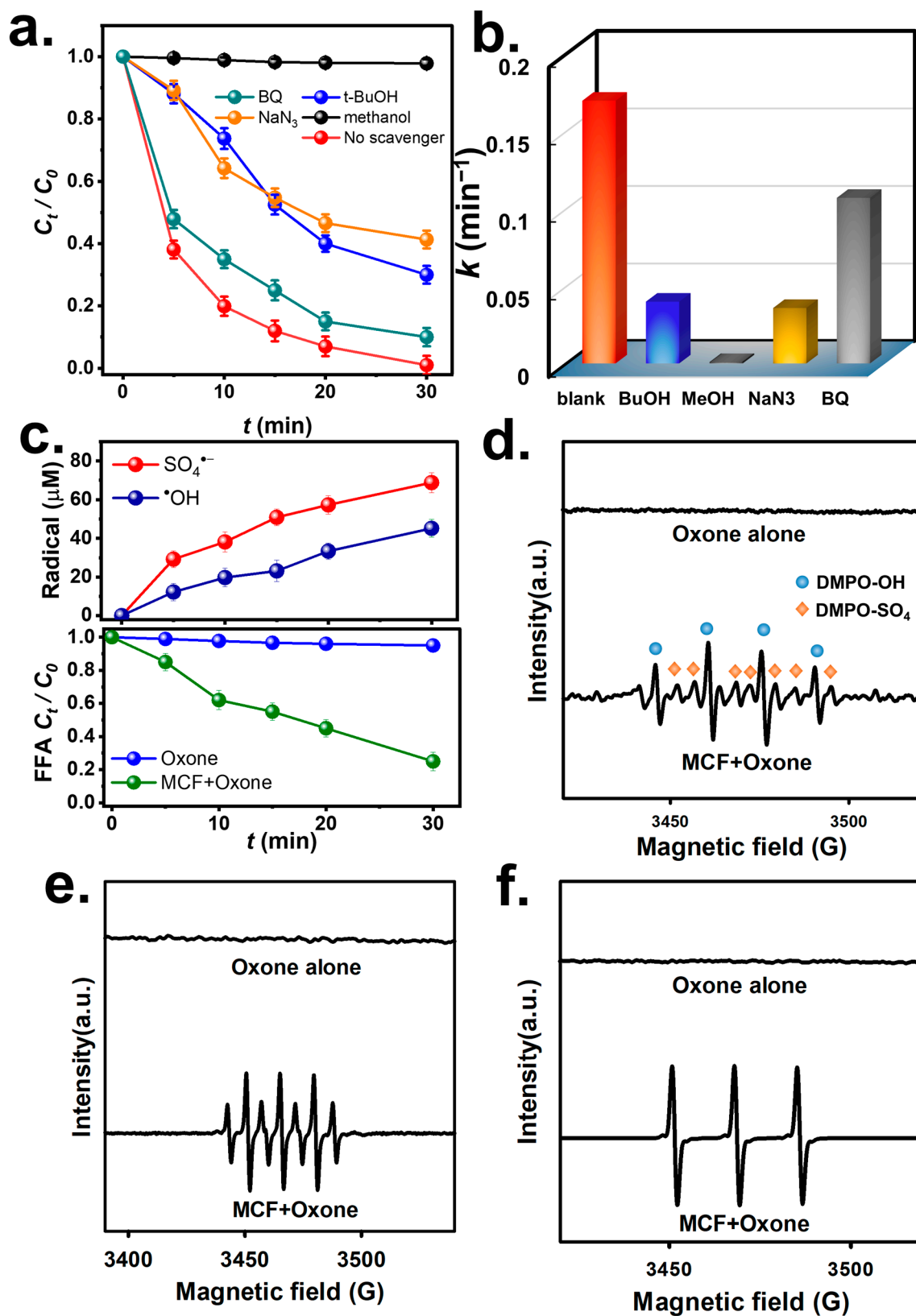
Figure 8. (**a**) Effects of various inhibitors and (**b**) corresponding rate constants; ESR analyses: (**c**) DMPO, (**d**) DMPO in methanol, (**e**) TEMP, (**f**) fractions of ROS; and FFA consumption by MCF + Oxone.

Moreover, electron spin resonance (ESR) was adopted here to determine radical species in the BHPM degradation. Firstly, when 5,5-Dimethyl-1-pyrroline N-oxide

(DMPO) was adopted, no noticeable feature was observed in the case of Oxone alone (Figure 8d). When DMPO, Oxone, and MCF were added simultaneously, a noticeable result was noted and attributed to DMPO-SO$_4$ and DMPO-OH, as displayed in Figure 8c, validating the existence of SO$_4^{\bullet-}$ and $^{\bullet}$OH. Moreover, the same test was then implemented in MeOH to examine whether O$_2^{\bullet-}$ was present (Figure 8e), and a notable signal was observed but it was ascribed to DMPO-X rather than DMPO-O$_2$, suggesting that the existence of O$_2^{\bullet-}$ was insignificant.

Furthermore, once an alternative spin-trapping agent 2,2,6,6-tetramethylpiperidine (TEMP) was used, no notable signal was seen for Oxone alone. However, after TEMP, Oxone, and MCF were all present, a huge signal was noted and attributed to TEMP-^{1}O$_2$ (Figure 8f), validating the presence of ^{1}O$_2$. Therefore, BHPM degradation can be attributed to SO$_4^{\bullet-}$, $^{\bullet}$OH, and ^{1}O$_2$ generated from MCF-activated Oxone, as outlined in Figure 9.
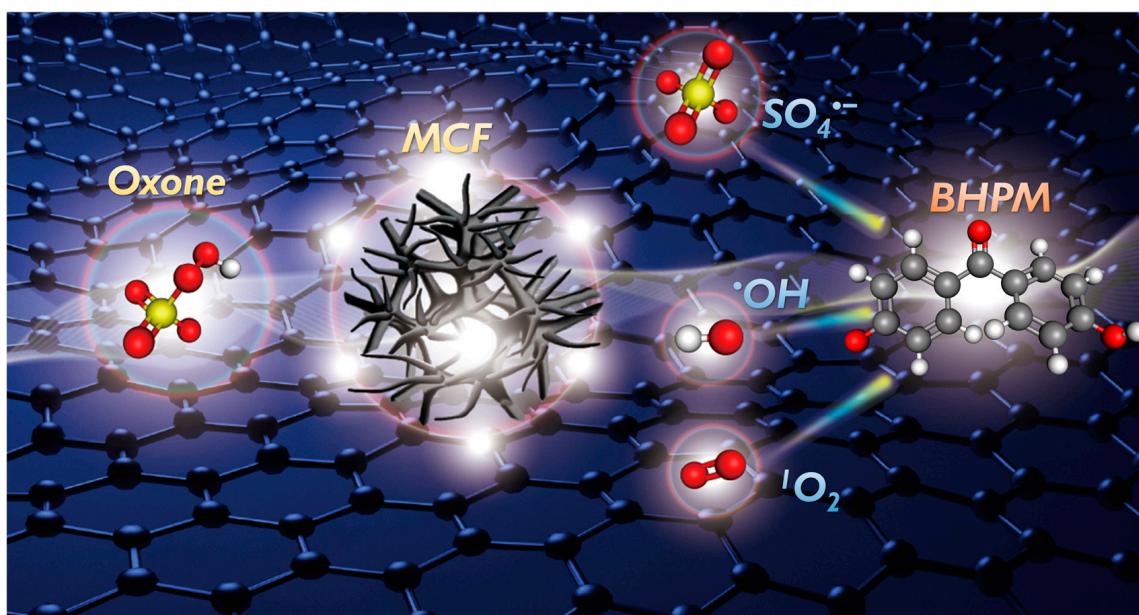
Figure 9. Illustration of the degradation mechanism of BHPM by MCF + Oxone.

3.5. Degradation Process of BHPM

Since MCF efficiently activated Oxone to eliminate the BHPM, it was profitable to further explore the BHPM degradation process. To this end, a First-Principle-based computation was used to evaluate the molecule-level susceptibility in the BHPM, and the optimal structural configuration of the BHPM was then computed, as in Figure 10a. Specifically, Figure 10b,c reveal the HOMO and the LUMO of the BHPM. Conventionally, the HOMO sites are prone to receiving electrophilic attacks as SO$_4^{\bullet-}$ and $^{\bullet}$OH would be recognized as electrophilic radicals and ^{1}O$_2$ is also an electrophilic. Therefore, the HOMO sites at the benzene group of the BHPM would possibly withdraw electrophilic attacks from the aforementioned species. Figure 10d further outlines the electrostatic potential (ESP)-distributed analysis of the BHPM, which indicates that the electron-abundant portions of the BHPM would be more probable regions to accept electrophilic attacks.
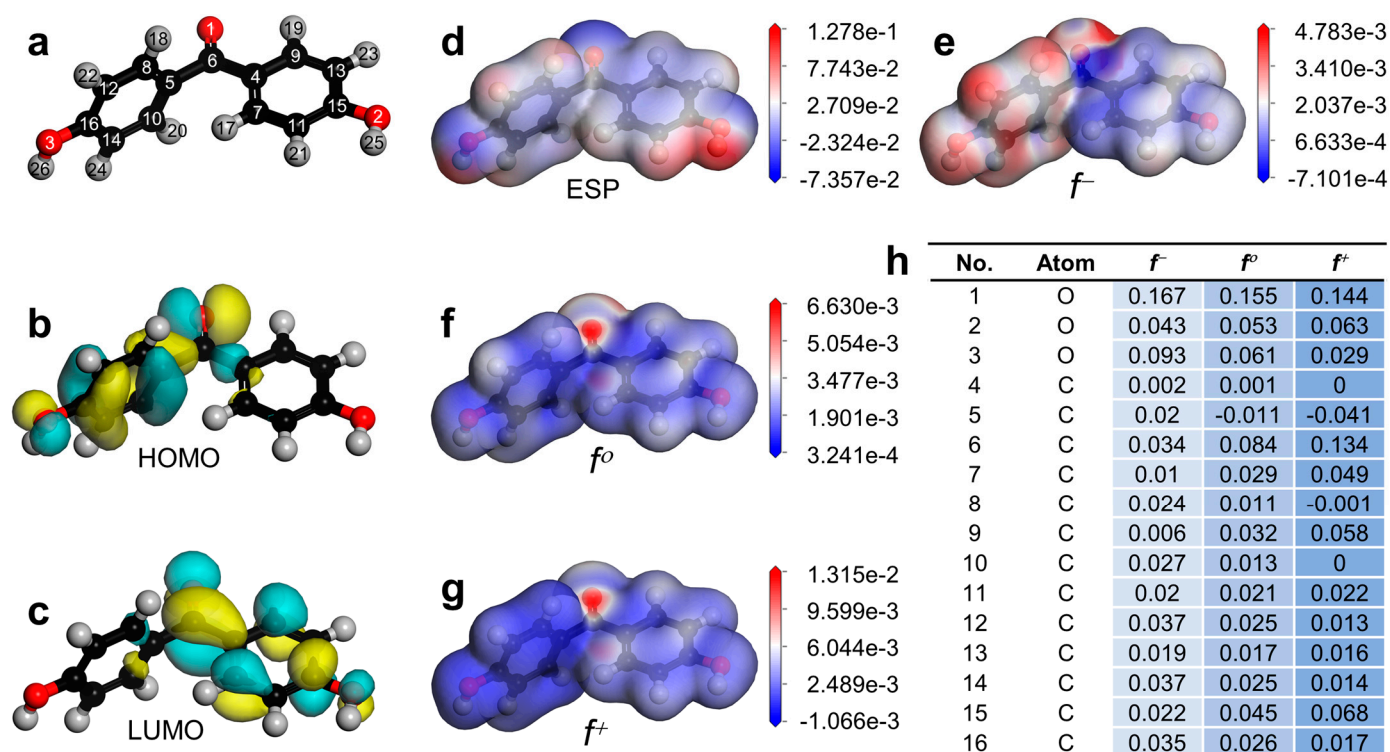
Figure 10. (**a**) Optimized structure of BHPM; (**b**,**c**) HOMO and LUMO; (**d**) ESP; (**e**–**g**) electron density mapped by f^-, f^0, f^+ (iso-surface value = 0.03 electrons/Å^3); and (**h**) Fukui indices of BHPM.

No.	Atom	f^-	f^0	f^+
1	O	0.167	0.155	0.144
2	O	0.043	0.053	0.063
3	O	0.093	0.061	0.029
4	C	0.002	0.001	0
5	C	0.02	-0.011	-0.041
6	C	0.034	0.084	0.134
7	C	0.01	0.029	0.049
8	C	0.024	0.011	-0.001
9	C	0.006	0.032	0.058
10	C	0.027	0.013	0
11	C	0.02	0.021	0.022
12	C	0.037	0.025	0.013
13	C	0.019	0.017	0.016
14	C	0.037	0.025	0.014
15	C	0.022	0.045	0.068
16	C	0.035	0.026	0.017

Moreover, in order to provide further details about possible sites of BHP for accepting attacks, the Fukui index of the BHPM was then quantified and is summarized in Figure 10h. Specifically, f^-, f^0, and f^+ denote electrophilic reaction, radical attack, and nucleophilic reaction, respectively. As $^1O_2$ is an intense electrophilic species, the sites of BHPM with larger indices of f-would be prone to receiving the electrophilic attacks. Therefore, O1, O3, C6, C12, C14, and C16 exhibited much larger f-indices, signifying that these positions would attract electrophilic attacks. Nevertheless, as O1 and O3 would be considered as saturated sites, C6, C12, and C14 may be relatively vulnerable sites for receiving primary attacks.

To elucidate the possible degradation pathway of the BHPM by MCF + Oxone, a mass spectrometry of BHPM degradation intermediates (Figure S5 and Table S2) was then acquired and integrated with the aforementioned information on computational chemistry to depict a possible degradation process in Figure 11. Initially, the benzene ring of the BHPM, where the HOMO is located, could receive a ring-opening attack to generate an intermediate, M1, which would then transform to M2 upon continuous oxidations. Next, M2 would be decomposed to eliminate the ring-opened residual group to produce M3, which would encounter continuous oxidations to afford M4. Upon further attacks, M4 would then be degraded by another ring-opening reaction to generate M5, which then would be consecutively decomposed to produce low-molecule-weight intermediates, such as M5, M6, and finally M7.
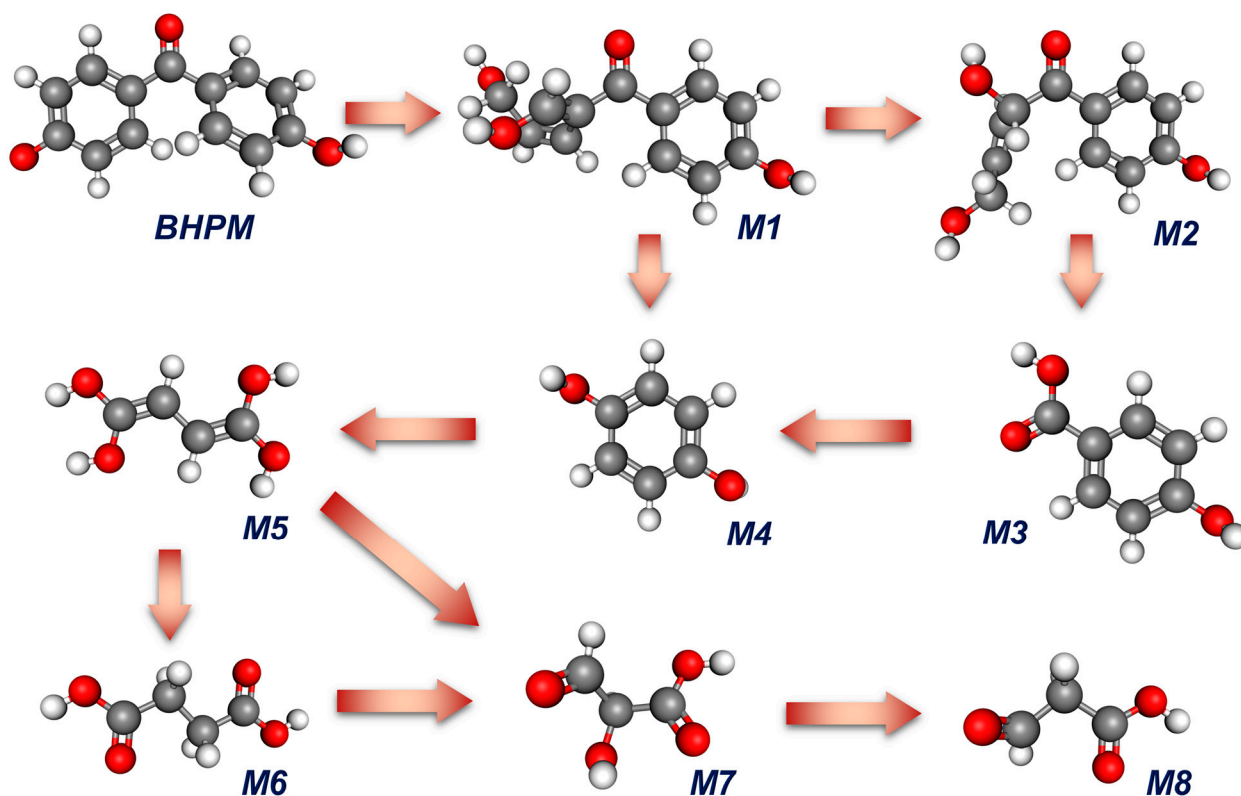
Figure 11. A proposed degradation process of BHPM based on the detected intermediates.

3.6. Eco-Toxicity Evaluation of BHP Degradation Intermediates

Given the degradation pathway of BHPM by MCF + Oxone, it was certainly imperative to probe into the eco-toxicity of these intermediates along the BHP elimination route for waterborne lives. Therefore, the Ecological Structure Activity Relationships (ECOSAR) Predictive Model was then employed to estimate the toxic properties of these degradation intermediates from BHPM in terms of acute toxicity ($LC50_{fish/daphnia}$ & $EC50_{green\ algae}$) and chronic toxicity ($ChV_{fish/daphnia/green\ algae}$), as in Figure 12a,b, respectively. According to the Globally Harmonized System of Classification and Labelling of Chemicals (Table S3), the data of LC_{50} of these intermediates from the ECOSAR could then be classified into the four toxic categories, including "very toxic", "toxic", "harmful", and "non-harmful". Figure 12a summarizes the values of Log LC50 of these intermediates as well as their classes. In the case of green algae, the toxicity of pristine BHPM was very high. After the BHP was decomposed, the toxicities of the initial intermediates (M1 and M2) dropped significantly, and then the toxicities gradually abated in the following intermediates of M3~M8.

Likewise, a similar pattern could also be observed using fish and daphnia as indicators because the initial toxicity of the BHPM was still very high, and it constantly dropped together with the degradation process. In the cases of chronic toxicities (Figure 12b), MCF + Oxone also enabled a substantial reduction in chronic toxicities for fish, daphnia, and green algae after the BHPM was continuously decomposed into low-molecule-weight intermediates.

These results demonstrate that while BHPM is toxic, its derivative intermediates by MCF + Oxone were mostly non-harmful, validating the theory that MCF + Oxone was advantageous to degrade BHPM without the occurrence of very toxic intermediates, and also decontaminate BHPM along the decomposition.
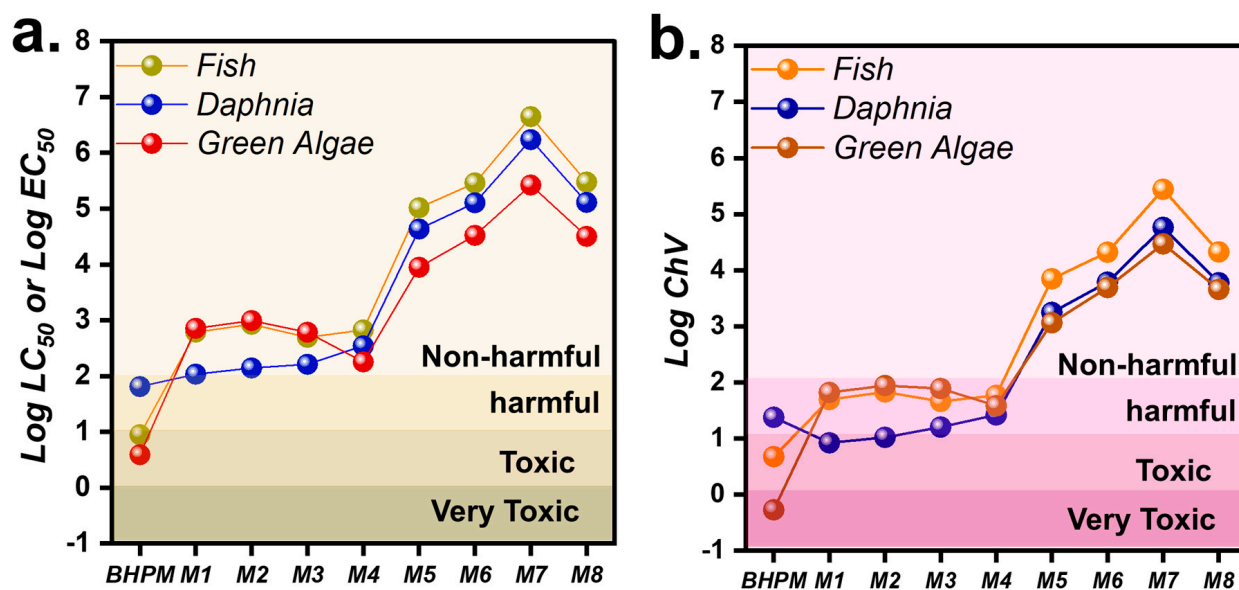
Figure 12. Eco-toxicity evaluation of BHPM degradation by the ECOSAR: (**a**) acute toxicities; (**b**) chronic toxicities.

4. Conclusions

In this study, MCF was fabricated by using melamine foam as a readily available precursor. Through the carbonization and deposition of Co/Fe-TA complexation, the nano-needle of the Co/Fe species was adorned onto the N-doped carbon foam, forming a magnetic 3D-structured carbonaceous catalyst. This resultant MCF exhibited superior textural properties, surficial active sites and enhanced electrochemical characteristics for accelerating Oxone activation in order to degrade an emerging contaminant, BHPM.

Furthermore, MCF + Oxone exhibited a lower activation energy for BHPM elimination and retained its effectiveness in eliminating the BHPM over multiple rounds. The BHPM degradation mechanism and pathway were also comprehensively investigated via experimental investigation and theoretical studies. More importantly, MCF + Oxone can successfully detoxify BHPM. These results render MCF a promising activator for Oxone to degrade BHPM.

Author Contributions: Data collection and draft, Y.-C.C. and X.-Y.J.; methodology, B.X.T. and H.W.; software, C.-W.H.; validation, J.-Y.L.; formal analysis, A.E.; data curation, S.S.; writing—original draft preparation, K.-Y.L.; writing—review and editing, H.Y. All authors have read and agreed to the published version of the manuscript.

Institutional Review Board Statement: Not applicable.

Informed Consent Statement: Not applicable.

Data Availability Statement: Data are contained within the article and supplementary materials.

Conflicts of Interest: The authors declare no conflict of interest.

References

1. Lin, K.-Y.A.; Lin, J.-T.; Lu, X.-Y.; Hung, C.; Lin, Y.-F. Electrospun magnetic cobalt-embedded carbon nanofiber as a heterogeneous catalyst for activation of oxone for degradation of Amaranth dye. *J. Colloid Interface Sci.* **2017**, *505*, 728–735. [CrossRef] [PubMed]
2. Alvi, S.; Jayant, V.; Ali, R. Applications of Oxone® in Organic Synthesis: An Emerging Green Reagent of Modern Era. *ChemistrySelect* **2022**, *7*, e202200704. [CrossRef]
3. Cui, K.-P.; He, Y.-Y.; Xu, K.-J.; Zhang, Y.; Chen, C.-B.; Xu, Z.-J.; Chen, X. Degradation of Tetracycline Hydrochloride by Cu-Doped MIL-101(Fe) Loaded Diatomite Heterogeneous Fenton Catalyst. *Nanomaterials* **2022**, *12*, 811. [CrossRef] [PubMed]
4. Eslami, A.; Mehdipour, F.; Lin, K.-Y.A.; Sharifi Maleksari, H.; Mirzaei, F.; Ghanbari, F. Sono-photo activation of percarbonate for the degradation of organic dye: The effect of water matrix and identification of by-products. *J. Water Process Eng.* **2020**, *33*, 100998. [CrossRef]
5. Kohantorabi, M.; Moussavi, G.; Giannakis, S. A review of the innovations in metal- and carbon-based catalysts explored for heterogeneous peroxymonosulfate (PMS) activation, with focus on radical vs. non-radical degradation pathways of organic contaminants. *Chem. Eng. J.* **2021**, *411*, 127957. [CrossRef]
6. Lin, K.-Y.A.; Lin, J.-T.; Jochems, A.P. Oxidation of amaranth dye by persulfate and peroxymonosulfate activated by ferrocene. *J. Chem. Technol. Biotechnol.* **2017**, *92*, 163–172. [CrossRef]
7. Gasim, M.F.; Lim, J.W.; Low, S.C.; Lin, K.Y.A.; Oh, W.D. Can biochar and hydrochar be used as sustainable catalyst for persulfate activation? *Chemosphere* **2022**, *287*, 132458. [CrossRef]
8. Yang, S.Y.; Wang, P.; Yang, X.; Shan, L.; Zhang, W.Y.; Shao, X.T.; Niu, R. Degradation efficiencies of azo dye Acid Orange 7 by the interaction of heat, UV and anions with common oxidants: Persulfate, peroxymonosulfate and hydrogen peroxide. *J. Hazard. Mater.* **2010**, *179*, 552–558. [CrossRef]
9. Zhang, B.T.; Xiang, W.X.; Jiang, X.M.; Zhang, Y.; Teng, Y.G. Oxidation of Dyes by Alkaline-Activated Peroxymonosulfate. *J. Environ. Eng.* **2016**, *142*, 04016003. [CrossRef]
10. Wei, G.L.; Liang, X.L.; He, Z.S.; Liao, Y.S.; Xie, Z.Y.; Liu, P.; Ji, S.C.; He, H.P.; Li, D.Q.; Zhang, J. Heterogeneous activation of Oxone by substituted magnetites Fe$_3$-xMxO$_4$ (Cr, Mn, Co, Ni) for degradation of Acid Orange II at neutral pH. *J. Mol. Catal. A-Chem.* **2015**, *398*, 86–94. [CrossRef]
11. Cai, C.; Zhang, H.; Zhong, X.; Hou, L. Ultrasound enhanced heterogeneous activation of peroxymonosulfate by a bimetallic Fe–Co/SBA-15 catalyst for the degradation of Orange II in water. *J. Hazard. Mater.* **2015**, *283*, 70–79. [CrossRef] [PubMed]
12. Giannakis, S.; Lin, K.-Y.A.; Ghanbari, F. A review of the recent advances on the treatment of industrial wastewaters by Sulfate Radical-based Advanced Oxidation Processes (SR-AOPs). *Chem. Eng. J.* **2021**, *406*, 127083. [CrossRef]
13. Anipsitakis, G.P.; Stathatos, E.; Dionysiou, D.D. Heterogeneous Activation of Oxone Using Co$_3$O$_4$. *J. Phys. Chem. B* **2005**, *109*, 13052–13055. [CrossRef] [PubMed]
14. Sun, J.; Li, X.; Feng, J.; Tian, X. Oxone/Co^{2+} oxidation as an advanced oxidation process: Comparison with traditional Fenton oxidation for treatment of landfill leachate. *Water Res.* **2009**, *43*, 4363–4369. [CrossRef] [PubMed]
15. Andrew Lin, K.-Y.; Hsu, F.-K. Magnetic iron/carbon nanorods derived from a metal organic framework as an efficient heterogeneous catalyst for the chemical oxidation process in water. *RSC Adv.* **2015**, *5*, 50790–50800. [CrossRef]
16. Adil, S.F.; Ashraf, M.; Khan, M.; Assal, M.E.; Shaik, M.R.; Kuniyil, M.; Al-Warthan, A.; Siddiqui, M.R.H.; Tremel, W.; Tahir, M.N. Advances in Graphene/Inorganic Nanoparticle Composites for Catalytic Applications. *Chem. Rec.* **2022**, *22*, e202100274. [CrossRef]
17. Xu, L.J.; Chu, W.; Gan, L. Environmental application of graphene-based CoFe$_2$O$_4$ as an activator of peroxymonosulfate for the degradation of a plasticizer. *Chem. Eng. J.* **2015**, *263*, 435–443. [CrossRef]
18. Liang, X.; Zhao, Y.; Liu, J.; Yang, Z.; Yang, Q. Highly efficient activation of peroxymonosulfate by cobalt ferrite anchored in P-doped activated carbon for degradation of 2,4-D: Adsorption and electron transfer mechanism. *J. Colloid Interface Sci.* **2023**, *642*, 757–770. [CrossRef]
19. Liu, Y.; Tao, F.; Xing, Y.; Pei, Y.; Ren, F. Melamine Foam-Derived Carbon Scaffold for Dendrite-Free and Stable Zinc Metal Anode. *Molecules* **2023**, *28*, 1742. [CrossRef]
20. Duan, X.G.; Sun, H.Q.; Wang, Y.X.; Kang, J.; Wang, S.B. N-Doping-Induced Nonradical Reaction on Single-Walled Carbon Nanotubes for Catalytic Phenol Oxidation. *ACS Catal.* **2015**, *5*, 553–559. [CrossRef]
21. Hu, H.; Guan, B.Y.; Lou, X.W. Construction of Complex CoS Hollow Structures with Enhanced Electrochemical Properties for Hybrid Supercapacitors. *Chem* **2016**, *1*, 102–113. [CrossRef]
22. Wang, Y.; Wei, X.; Hu, X.; Zhou, W.; Zhao, Y. Effect of Formic Acid Treatment on the Structure and Catalytic Activity of Co$_3$O$_4$ for N$_2$O Decomposition. *Catal. Lett.* **2019**, *149*, 1026–1036. [CrossRef]
23. Li, G.; Sun, J.H.; Hou, W.P.; Jiang, S.D.; Huang, Y.; Geng, J.X. Three-dimensional porous carbon composites containing high sulfur nanoparticle content for high-performance lithium-sulfur batteries. *Nat. Commun.* **2016**, *7*, 10601. [CrossRef] [PubMed]
24. Hasan, Z.; Cho, D.W.; Chon, C.M.; Yoon, K.; Song, H. Reduction of p-nitrophenol by magnetic Co-carbon composites derived from metal organic frameworks. *Chem. Eng. J.* **2016**, *298*, 183–190. [CrossRef]
25. He, P.; Wu, Y.; Chen, H.; Zhu, Z.; Liu, H.; Gao, J.; Xu, H. Hierarchical bimetal embedded in carbon nanoflower electrocatalysts derived from metal-organic frameworks for efficient oxygen evolution reaction. *J. Alloys Compd.* **2020**, *813*, 152192. [CrossRef]
26. Liu, D.; Wu, C.; Yan, M.; Wang, J. Correlating the microstructure, growth mechanism and magnetic properties of FeSiAl soft magnetic composites fabricated via HNO$_3$ oxidation. *Acta Mater.* **2018**, *146*, 294–303. [CrossRef]

27. Osadchii, D.Y.; Olivos-Suarez, A.I.; Bavykina, A.V.; Gascon, J. Revisiting Nitrogen Species in Covalent Triazine Frameworks. *Langmuir* **2017**, *33*, 14278–14285. [CrossRef]

28. Jiang, X.-Y.; Park, Y.-K.; Wen, J.-C.; Bui, H.M.; Lin, Y.-F.; Sirivithayapakorn, S.; Khiem, T.C.; Munagapati, V.S.; Lin, K.-Y.A. Hollow-architected Co_3O_4 for enhancing Oxone activation to eliminate an anesthetic, benzocaine, from water: A structure-property investigation with degradation pathway and eco-toxicity. *J. Taiwan Inst. Chem. Eng.* **2023**, *150*, 105042. [CrossRef]

29. Miao, J.; Geng, W.; Alvarez, P.J.J.; Long, M. 2D N-Doped Porous Carbon Derived from Polydopamine-Coated Graphitic Carbon Nitride for Efficient Nonradical Activation of Peroxymonosulfate. *Environ. Sci. Technol.* **2020**, *54*, 8473–8481. [CrossRef]

30. Liu, Z.; Sun, X.; Sun, Z. CoNi alloy anchored onto N-doped porous carbon for the removal of sulfamethoxazole: Catalyst, mechanism, toxicity analysis, and application. *Chemosphere* **2022**, *308*, 136291. [CrossRef]

31. Sun, X.; Qi, H.; Mao, S.; Sun, Z. Atrazine removal by peroxymonosulfate activated with magnetic CoFe alloy@N-doped graphitic carbon encapsulated in chitosan carbonized microspheres. *Chem. Eng. J.* **2021**, *423*, 130169. [CrossRef]

32. Cong Khiem, T.; Duan, X.; Liu, W.-J.; Park, Y.-K.; Manh Bui, H.; Oh, W.-D.; Ghotekar, S.; Fai Tsang, Y.; Andrew Lin, K.-Y. MOF-templated Hollow Cobalt Sulfide as an Enhanced Oxone Activator for Degradation of UV Absorber: Key Role of Sulfur Vacancy-Induced Highly Active CoII Sites. *Chem. Eng. J.* **2022**, *453*, 139699. [CrossRef]

33. Yuan, R.; Yin, X.; Gu, S.; Chang, J.; Li, H. Flexible double-wall carbon foam/Cu-Co oxides based symmetric supercapacitor with ultrahigh energy density. *J. Mater. Sci. Technol.* **2023**, *160*, 109–117. [CrossRef]

34. Li, Y.; Li, F.-M.; Meng, X.-Y.; Li, S.-N.; Zeng, J.-H.; Chen, Y. Ultrathin Co_3O_4 Nanomeshes for the Oxygen Evolution Reaction. *ACS Catal.* **2018**, *8*, 1913–1920. [CrossRef]

35. Yue, L.; Zhang, S.; Zhao, H.; Feng, Y.; Wang, M.; An, L.; Zhang, X.; Mi, J. One-pot synthesis $CoFe_2O_4$/CNTs composite for asymmetric supercapacitor electrode. *Solid State Ion.* **2019**, *329*, 15–24. [CrossRef]

36. Othman, I.; Hisham Zain, J.; Abu Haija, M.; Banat, F. Catalytic activation of peroxymonosulfate using $CeVO_4$ for phenol degradation: An insight into the reaction pathway. *Appl. Catal. B* **2020**, *266*, 118601. [CrossRef]

37. Liu, W.-J.; Yang, H.; Park, Y.-K.; Kwon, E.; Huang, C.-W.; Thanh, B.X.; Khiem, T.C.; You, S.; Ghanbari, F.; Lin, K.-Y.A. Enhanced degradation of ultra-violet stabilizer Bis(4-hydroxy)benzophenone using oxone catalyzed by hexagonal nanoplate-assembled CoS 3-dimensional cluster. *Chemosphere* **2022**, *288*, 132427. [CrossRef]

38. Guo, W.; Su, S.; Yi, C.; Ma, Z. Degradation of antibiotics amoxicillin by Co_3O_4-catalyzed peroxymonosulfate system. *Environ. Prog. Sustain. Energy* **2013**, *32*, 193–197. [CrossRef]

39. Zhang, T.; Chen, Y.; Wang, Y.; Le Roux, J.; Yang, Y.; Croué, J.-P. Efficient Peroxydisulfate Activation Process Not Relying on Sulfate Radical Generation for Water Pollutant Degradation. *Environ. Sci. Technol.* **2014**, *48*, 5868–5875. [CrossRef]

40. Mostafa, S.; Rosario-Ortiz, F.L. Singlet oxygen formation from wastewater organic matter. *Environ. Sci. Technol.* **2013**, *47*, 8179–8186. [CrossRef]